PAPER PB

Spatial Bandwidth Limitations of Seismic Geotomography

Jerry M. Harris

ABSTRACT

Geotomography uses waves to image subsurface features of the Earth. Several practical considerations restrict the angles at which projections can be measured. Unlike medical tomography, geotomography is limited because sources and receivers are restricted to boreholes and the Earth's surface. Also, due to high attenuation rates in rocks, the frequency bandwidth of geotomography signals is severely restricted. In this paper, I summarize these limitations in terms of the Fourier support region, e.g., bandwidth, sampled by the ideal reconstruction algorithm. To identify the region of Fourier support, I apply a phenomenological interpretation to the theory of diffraction tomography based on the Born approximation. Three important geophysical applications are considered: (1) surface-to-surface reflection imaging; (2) offset vertical seismic profiling; and (3) and crosswell seismic profiling. Earlier work on this subject has comprehensively addressed limited-view scalar waves at a single frequency. In this paper, I cover both scalar and vector waves observed with limited view and multiple frequencies. I describe how multiple frequencies complement and can be exchanged for multiple views. I describe how the spatial bandwidth required for imaging is achieved with "apparent" wavelengths, which are the projections of the longitudinal wavelength onto the object heterogeneity. These apparent wavelengths are obtained by varying the angle of incidence, angle of observation, the frequency, and in some cases the polarization of the probing waves.

INTRODUCTION

Tomography reconstructs an object profile from its measured projections. The conventional reconstruction is based on the projection-slice theorem or central-section theorem [1], which states that the Fourier transform of the projections at the angle θ in object space (x, z) is a slice at angle θ in (k_x, k_z) Fourier transform space. The projections in x-ray medical imaging are directly measured and usually correspond to transmission attenuation along a straight geometrical path connecting the source and receiver. With ultrasound [2, 3], however, a probing acoustic wave experiences, in addition to attenuation, both refraction and diffraction, the effects of which complicates the interpretation of geometric projections for use a reconstruction algorithm. This complication has been extensively discussed in the literature on diffraction tomography. Mueller [2], Greenleaf [3], and most recently Devaney [4, 5] have shown, using the Born and Rytov approximations, the effects of finite wavelength diffraction on image reconstruction. Examples have been taken from both medical and geophysical applications.

The term geotomography is used here to describe tomography applied to inversion problems in geophysics. Geotomography uses seismic (or electromagnetic) waves to image subsurface features of the earth. Unlike established x-ray transmission tomography, geotomography is more limited because sources and receivers are restricted to boreholes and the Earth's surface. This is due to the unusual imaging geometry experienced in the geophysical applications. In Figure 1, I illustrate the three standard geophysical configurations, namely (1) surface-to-surface reflection imaging, (2) offset vertical seismic profiling, and (3) crosswell seismic profiling. The major effect of these geometries is to limit the angles at which geotomographic projections can be measured. Devaney [5] was the first to illustrate the limitations for vertical seismic profiling and crosswell seismic profiling. However, Devaney only considered single frequency with multiple views and did not consider variations in the other available parameters.

The Earth is heterogeneous at nearly every scale one chooses to look. Therefore the geological spectrum is very broad. Nevertheless, the Fourier spectrum of the heterogeneities is appreciably different from zero only in some finite region of (k_x, k_z) Fourier space. Geotomography samples portions of this geological spectrum. Throughout the paper, I use the term spatial bandwidth to describe the support region in

the object's Fourier space that is sampled by geotomography. A narrow bandwidth resolves only large scale geological structure (low resolution) whereas a wide spatial bandwidth resolves small scale geological structure (high resolution). Obviously, one seeks to achieve the broadest bandwidth possible, thus assuring a highly resolved image of the geology. Figures throughout the paper illustrate the areas of the geological spectrum sampled by the various geotomography geometries.

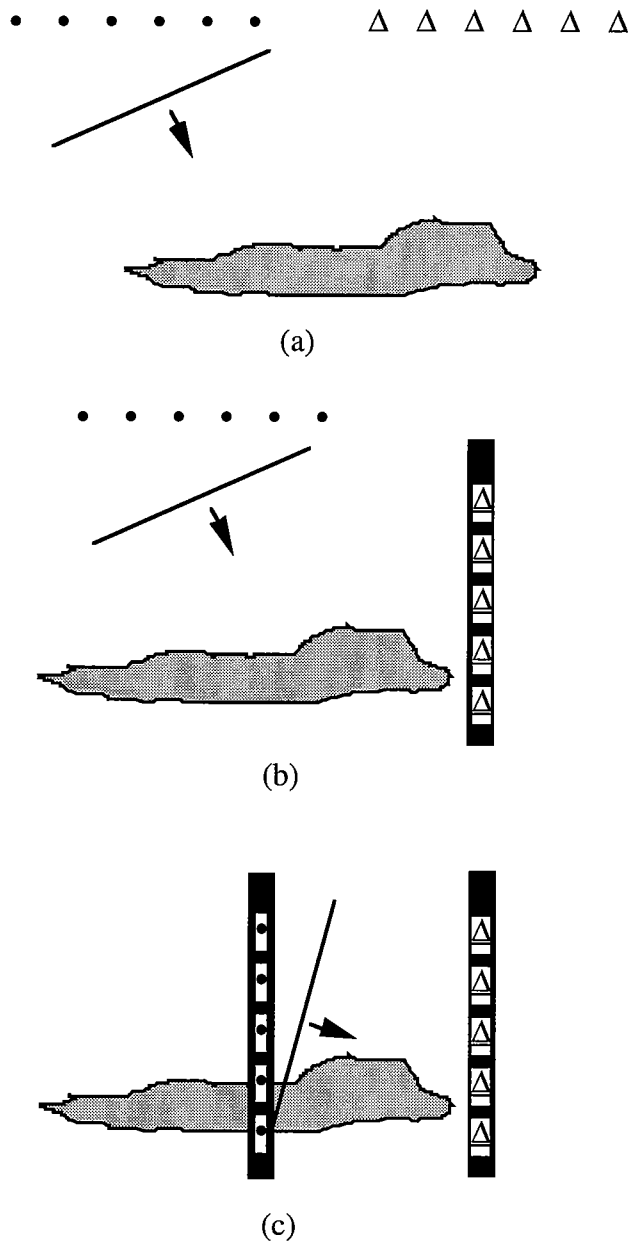

Figure 1. Conventional source and receiver configurations of geotomography: (a) surface seismic profiling; (b) vertical seismic profiling; (c) crosswell seismic profiling.

There are three independent parameters important to geotomographic imaging. These are the angle of incidence, angle of observation, and the wavelength of the probing radiation. In most of the published studies to date[2, 3, 4, 5, 7], variations in only two of the three (angle of incidence and angle of observation) were studied. One exception is the paper by Kenue and Greenleaf [6] in which limited-view multi-frequency reconstruction for medical applications were reported. Kenue, however, did not discuss spatial bandwidth in his paper but concentrated on the reconstruction algorithm. In the case of scalar waves, e.g., acoustics, the way to vary the third parameter, wavelength, is to vary the frequency. With vector waves, e.g., elastic or seismic waves, there are two (at least) distinct velocities of propagation in homogeneous media; therefore the wavelength can be varied without varying frequency but by changing the polarization of the wave.

In this paper, I examine the spatial bandwidth limitations imposed by limited view, limited signal frequency, and alternative polarization selection. I combine a phenomenological description of scattering with the theory of diffraction tomography. This approach provides a convenient method for describing elastic as well as acoustic waves. The paper is divided in to several parts. First, I describe the equations of the underlying mathematics for weak scattering of scalar waves in the Born and Rytov approximations. I emphasize an interpretation of the scattering physics. Next, I address reconstruction by diffraction tomography. The spatial spectra obtained from geotomography is covered in the following subsections. Elastic waves are briefly discussed in the final section.

WEAK SCATTERING OF SCALAR WAVES

I do not present an extensive derivation of scattering and diffraction tomography here. Instead, the reader is referred to the many excellent articles on the subject, e.g., [4, 5, 7, 8, 9]. What follows, however, is a brief review of the key results of the derivation and a phenomenological description of wave physics. The notation used here is identical to that shown in [9]. Scalar waves are discussed first, followed by vector elastic waves.

I begin with the reduced wave equation for the time-harmonic scalar waves in a three dimensional medium, i.e.,

$$(\nabla^2 + k^2)\, U(\mathbf{r},\omega) = k^2\, O(\mathbf{r}) U(\mathbf{r},\omega) \qquad (1)$$

where U ($\mathbf{r}$, w) is the total field observed at the position $\mathbf{r}$ = (x, y, z) due to a source outside the scattering volume, O($\mathbf{r}$) is the scattering volume which I seek with tomographic inversion. The object profile is imbedded in a homogeneous background medium whose wavenumber is k = ω/C. It is nonzero only inside the scattering volume. The object profile is related to the velocity of propagation through the equation

$$O(\mathbf{r}) = 1 - C_o^2 / C^2(\mathbf{r}). \tag{2}$$

The Fourier transform can be used to obtain time-dependent fields via the equation

$$U(\mathbf{r},t) = \int d\omega\, U(\mathbf{r},\omega) \exp(+i\omega t). \tag{3}$$

Throughout the paper, however, I will deal with time-harmonic fields only. As a result, the explicit designation of frequency will be suppressed in order to simplify the notation.

The well-known integral solution for the time-harmonic field U($\mathbf{r}$) described by the differential equation is

$$U(\mathbf{r}) = U_o(\mathbf{r}) + k^2 \int d\mathbf{r}'\, O(\mathbf{r}')U(\mathbf{r}')G_o(\mathbf{r},\mathbf{r}') \tag{4}$$

where $G_o(\mathbf{r}, \mathbf{r}') = \exp(ikR)/4\pi R$ is the Green's function for the background medium and $U_o(\mathbf{r})$ is the field in the absence of scattering, i.e., the field when O($\mathbf{r}$) = 0. As usual, I identify the integral term in equation (2.4) as the scattered field, i.e., $U_{sc} = U(\mathbf{r}) - U_o(\mathbf{r})$.

I consider U($\mathbf{r}$) in the far-field approximation. The far-field corresponds to observation points much larger than the dimension of the object profile. In such a case, the factor 1/R of the Green's functions can be approximated by 1/r and the phase is obtained by expanding R in a binonial series and keeping only the first term:

$$R = |\mathbf{r} - \mathbf{r}'| = (r^2 + r'^2 - 2r\mathbf{r}'\cdot\hat{\mathbf{s}})^{1/2} \cong r - \mathbf{r}'\cdot\hat{\mathbf{s}} \tag{5}$$

For large values of r the Green's function becomes

$$G_o(\mathbf{r},\mathbf{r}') = (4\pi r)^{-1} \exp(ikr - ik\mathbf{r}'\cdot\hat{\mathbf{s}}) \tag{6}$$

Substituting (6) into (4), I obtain an integral expression for the far-field scattered waves:

$$U_{sc}(\mathbf{r}) = A(\hat{\mathbf{s}},\hat{\mathbf{s}}')\exp(ikr)/r \tag{7}$$

$$A(\hat{\mathbf{s}},\hat{\mathbf{s}}') = k^2 \int d\mathbf{r}'\, O(\mathbf{r}')\exp(-ik\hat{\mathbf{s}}'\cdot\mathbf{r}') \tag{8}$$

Eqn. (8) is an exact expression for the far-field scattering amplitude $A(\hat{\mathbf{s}},\hat{\mathbf{s}}')$. Unfortunately, it is not possible to evaluate it because of the unknown total field $U(\mathbf{r})$ in the integrand. When scattering is weak, there are two popular and valid approximate solutions, the Born and Rytov approximations. Both were discussed by Harris [9] and Slaney [10] in connection with diffraction tomography. The fields estimated by the two approximations are related through a simple formula[9]. Therefore, I will continue here with results from the Born approximation only.

In the Born approximation, the field inside the scattering volume or object profile is approximated by the background field:

$$U(\mathbf{r}') \approx U_o(\mathbf{r}') = U_o \exp(ik\hat{\mathbf{s}}'\cdot\mathbf{r}') \tag{9}$$

Substituting (9) into (8), I obtain

$$A(\hat{\mathbf{s}},\hat{\mathbf{s}}') = k^2(4\pi)^{-1}U_o\, O(\mathbf{k}_s) \tag{10}$$

$$O(\mathbf{k}_s) = \int d\mathbf{r}'\, O(\mathbf{r}')\exp(-i\mathbf{k}_s\cdot\mathbf{r}') \tag{11}$$

where $\mathbf{k}_s = k(\hat{\mathbf{s}} - \hat{\mathbf{s}}')$, and the magnitude is $|\mathbf{k}_s| = 2\sin(\theta/2)$ and θ is the angle between $\hat{\mathbf{s}}'$ and $\hat{\mathbf{s}}$. See Figure 2.

For the purposes of this paper, the most important quantity is $O(\mathbf{k}_s)$ of Eqn. (11), which I call the shape factor. It contains all the geometry information about the scattering

object. I note that $O(\mathbf{k}_s)$ is the 3-D Fourier transform of the object profile in the direction $(\hat{\mathbf{s}}\text{-}\hat{\mathbf{s}}')$. The scattering vector $\mathbf{k}_s$ accounts for the relative phase among the elementary scattering volumes comprising the total volume. For this reason, the phenomena described by Eqns. (10) and (11) is very simple: each elementary volume $d\mathbf{r}'$ provides Rayleigh scattering independently of other elementary volumes. In a given direction, the waves interfere because of the different positions of the elementary volumes. Thus, the function of the scattering vector is to reference the relative phases of the elementary waves to a common origin. The magnitude of the scattering vector depends on the location of the scattering point $\mathbf{r}'$ and the scattering angle θ. The diagram in Figure 2 is helpful in explaining the construction. Let "P" denote an arbitrary origin and $\mathbf{r}'$ the vector to the scattering volume $d\mathbf{r}'$. The scalar pathlength from a plane wave source to $d\mathbf{r}'$ is longer by an amount $k\hat{\mathbf{s}}'\cdot\mathbf{r}'$ than the pathlength to the origin. Similarly, the pathlength traveled by the scattered wave from $d\mathbf{r}''$ is shorter by an amount $k\hat{\mathbf{s}}\cdot\mathbf{r}'$ than from P. Therefore, the total phase lag for scattering from $d\mathbf{r}'$ relative to scattering from P is $k(\hat{\mathbf{s}}' - \hat{\mathbf{s}})\cdot\mathbf{r}'$. The full magnitude of this phase vector is directed along the bisectrix of $\hat{\mathbf{s}}$ and $-\hat{\mathbf{s}}'$ for scalar wave scattering.

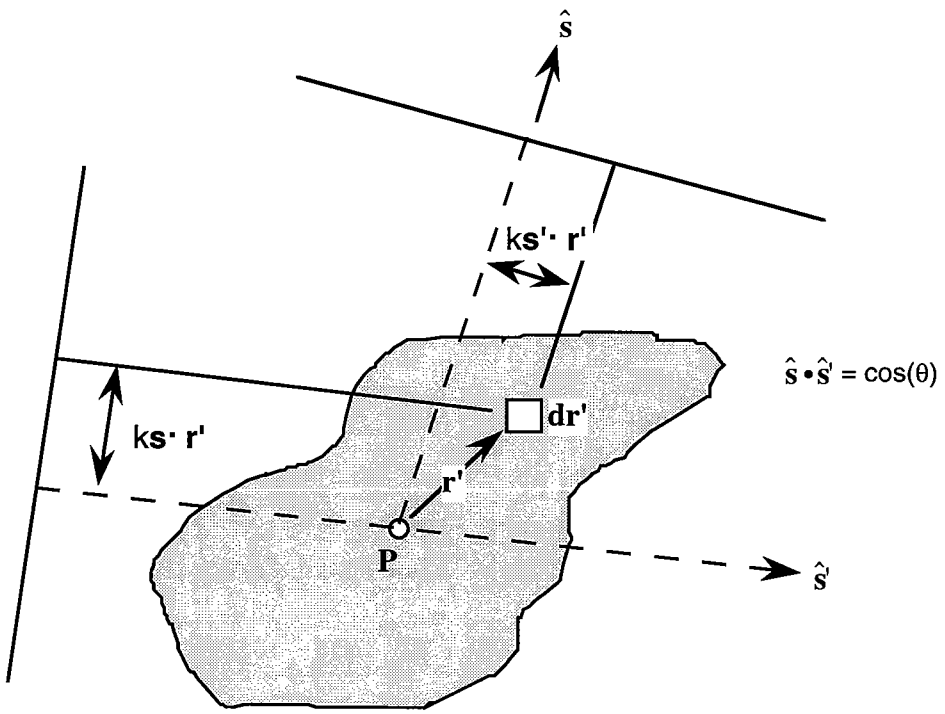

Figure 2. Scattering geometry for an incident plane wave propagating in the direction $\hat{\mathbf{s}}'$ and scattered in the direction $\hat{\mathbf{s}}$. Scattering described by Eqn. (12) is constructed from the relative phases illustrated.

DIFFRACTION TOMOGRAPHY

The goal of diffraction tomography is to sample the object's Fourier spectrum $O(\mathbf{k}_s)$ then invert the spectrum for the profile. Samples of the spectrum are obtained by varying $\mathbf{k}_s$, which translates into variations in $\hat{\mathbf{s}}$ the observation direction, $\hat{\mathbf{s}}'$ the incidence direction, or ω. Holding the frequency and incidence angle constant and varying the observation angle gives samples in Fourier space along a circular arc as shown in Figure 3a. This procedure is called single frequency multi-view sampling, the conventional way in which diffraction tomography is implemented. Alternatively, holding both $\hat{\mathbf{s}}$ and $\hat{\mathbf{s}}'$ constant and varying ω gives samples along a radial line as shown in Figure 3b, called multi-frequency sampling. The latter procedure produces samples along a straight line through the origin in the Fourier spectrum in a manner similar to the slice in conventional projection tomography. It is clear that with an appropriate set of incident and observation angles and frequencies, one can completely sample the object's spectrum and a suitable inversion is guaranteed.

Nevertheless, the problem with geotomography is the restriction placed on the allowed locations of sources and receivers. These restrictions limit the range of incidence and observation angles while intrinsic attenuation in the rocks limit the frequency of the signals that can be recorded. The combined result can large unsampled gaps in the Fourier spectrum; the specific locations of these gaps are discussed in the next section. These gaps can lead to severe artifacts in the reconstruction.

The general features of geotomography spectra can be illustrated with examples from scalar wave scattering Eqns. (10) - (13). In the examples that follow, the illustrations show the sample space or support region of the sampled spectrum, not the complex amplitude of the spectrum itself. I restrict the illustrations to 2D corresponding to data collection confined to a plane. The axes on the figures are labeled k_z and k_x for depth and offset wavenumbers, respectively. These wavenumbers represent the 2D components of the scattering vector $\mathbf{k}_s = k_x\hat{\mathbf{z}} + k_x\hat{\mathbf{x}}$. corresponding to the geological spectrum.

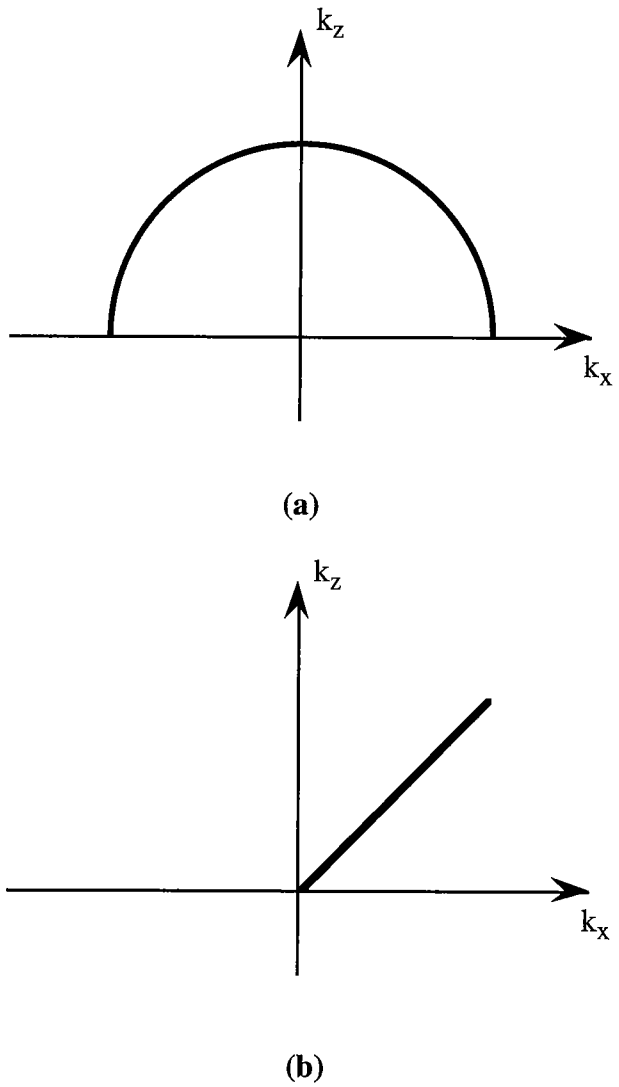

Figure 3. Lines in Fourier space sampled by (a) multi-view single frequency observations and (b) single-view multi-frequency observations.

All figures displaying spectra are normalized so that the maximum value $k_{max} = \left(k_x^2 + k_z^2\right)^{1/2}$ is shown full scale. Normalizing the scales in this manner can be a little misleading. For the three geophysical configurations, normalization in the display visually suggests that the maximum value of spatial frequency is the same or that the frequency content of the signals is the same for all cases. In fact, the frequency band of observed signals will be considerably different in the three applications. For comparison purposes, the bandwidth of surface reflections might be 5-50 Hz, for vertical seismic profiling 5-100 Hz,, and crosswell seismic profiling 50-1000 Hz. These differences, for

example, would yield an absolute value of spatial bandwidth for crosswell which an order of magnitude larger than surface-to-surface imaging. Thus, the illustrations which follow would need calibration in absolute scales for comparisons of absolute resolution or spatial bandwidth.

The first example, shown in Figures 4a and 4b, is taken from a medical application. It illustrates the differences between multi-view at a single frequency and limited-view with multiple frequencies. The rings in Figure 4a were obtained at a single frequency with constant angular offset between incidence and observation directions. That is, $\cos(\theta)= \hat{\mathbf{s}}\cdot\hat{\mathbf{s}}'$ (angle offset) is held constant while $\hat{\mathbf{s}}'$ is varied from 0 to 360 degrees, or all the way around the object profile. The radius of the various rings is given by $|\mathbf{k}_s| = 2k\sin(\theta/2)$ and the largest diameter ring correspond to backscattering, i.e., θ =180 degrees. The samples are evenly distributed in angle but unevenly distributed in the radial direction because of the trigonometric relationship between k_x and k_z and θ. The inverse Fourier transform is most easily implemented in Cartesian coordinates; therefore, polar sampling of this type can lead to reconstruction problems [1].

If multiple frequencies are used, samples are uniformly spaced in both radial and angle directions, as shown in Figure 4b. This example, called multi-view-multi-frequency monostatic backscattering, is obtained by holding θ = 180 degrees, varying $\hat{\mathbf{s}}'$ from 0 to 360 degrees, and varying the temporal frequency ω. As discussed above, maximum spatial frequency is achieved at the highest temporal frequency.

This simple example clearly illustrates how multi-view and multi-frequency measurements can be exchanged while sampling the same area in Fourier space. However, it is important to realize that the two methods are equivalent only when the simplifying assumptions are valid. Namely, the weak scattering approximation must hold, and the material properties of the object profile must not depend explicitly on frequency over the range of angle or frequency measurement, i.e., isotropic and non-dispersive media. While other considerations may suggest distinct advantages for one over the other, a combination of both multi-view and multi-frequency will usually be the compromise when noise and acquisition limitations are present.

This example also illustrates how he important variable for imaging is spatial bandwidth. Spatial bandwidth can be obtained with multi-view or multi-frequency

sampling via variations in $\mathbf{k}_s$ by probing the object with a spectrum of "apparent" wavelengths. In some cases, a measurement restriction in one may be overcome by measurements of the other. In the next section, examples illustrating the natural restrictions imposed by geotomography configurations are given.

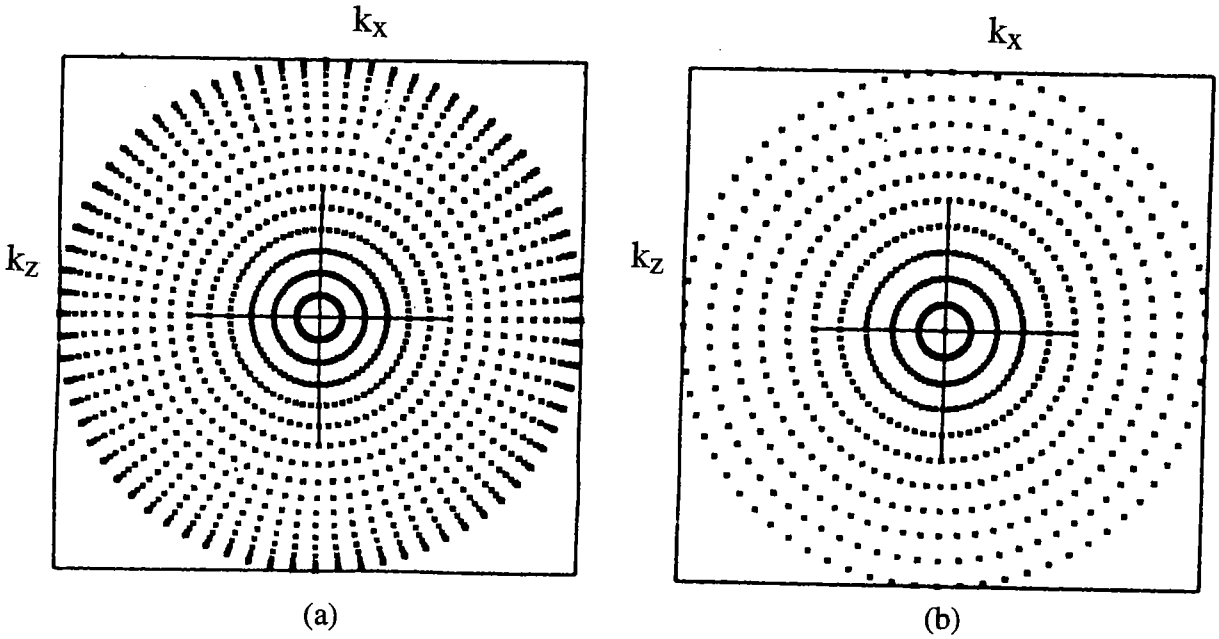

Figure 4. Full aperture imaging is possible in medical applications. (a) multi-view at a single frequency and (b) multi-view mono-static backscattering (θ=180 deg.) with multiple frequencies.

SPATIAL SPECTRA

In this section, I illustrate the sampled spectra obtained form the standard configurations of geotomography. The results are categorized by application, i.e., source/receiver configuration. One final point: The Fourier spectrum of purely real object profiles possesses reflection symmetry, that is, $O(\mathbf{k}_s) = O(-\mathbf{k}_s)$. Therefore, it is possible, at least theoretically, to expand the area of Fourier support sampled when this condition is met. Devaney [5] uses this property in his diffraction tomography reconstruction algorithm.

SURFACE REFLECTIONS

The configuration of sources and receivers in surface-to-surface reflection seismology is shown in Figure 1a. A typical spatial spectrum for single frequency multi-view observations is shown in Figure 5a. This display was generated using 0 to 180 degrees of illumination and 0 to 180 degrees of backscattered (reflected) observations. The samples near the origin correspond to small angle forward scattering which is this case are direct arrivals for incident and observation angles near 0 degrees or 180 degrees. In practice where it is impossible to achieve a full semicircle of illumination or observation, the coverage would span a sub-section of Figure 5a. Although I have a single frequency measurement, notice that the spectrum contains samples near the origin as well as at $k_{max} = 2k$. This shows that low spatial frequency (long wavelength) structure can be sampled provided incident and observation vectors with large horizontal wavenumbers are utilized. In such cases, the apparent vertical wavelength becomes very long.

The multi-frequency spectrum is shown in Figure 5b. By changing the frequency and keeping the same set of multiple views used in Fig. 6a, one effectively reproduces the pattern of Figure 5a but with a scaled radial magnitude. In this case, I can effectively complete the entire upper half plane with the multi-frequency and multi-view samples. This example highlights another benefit of multi-frequency measurements, which is to fill in blind spots in the single frequency multi-view coverage. Because changes in frequency provide Fourier space samples along a radial line, multi-frequency measurements can be used to fill gaps which occur between a multi-view samples and the origin. This example also illustrates how broadband signals are "required" to sample the low frequency vertical structure in surface seismology.

Another surface-to-surface technique is to measure multi-frequency monostatic backscattering only, i.e., co-located source and receiver or single-fold data or sonar-like data. At a single frequency, one would obtain a spectrum which consists of single ring as shown in Figure 5c. Multiple frequencies could be used to reduce the radius of this ring to a value as close to origin as practical, yielding the sample spectrum shown in Figure 5d.

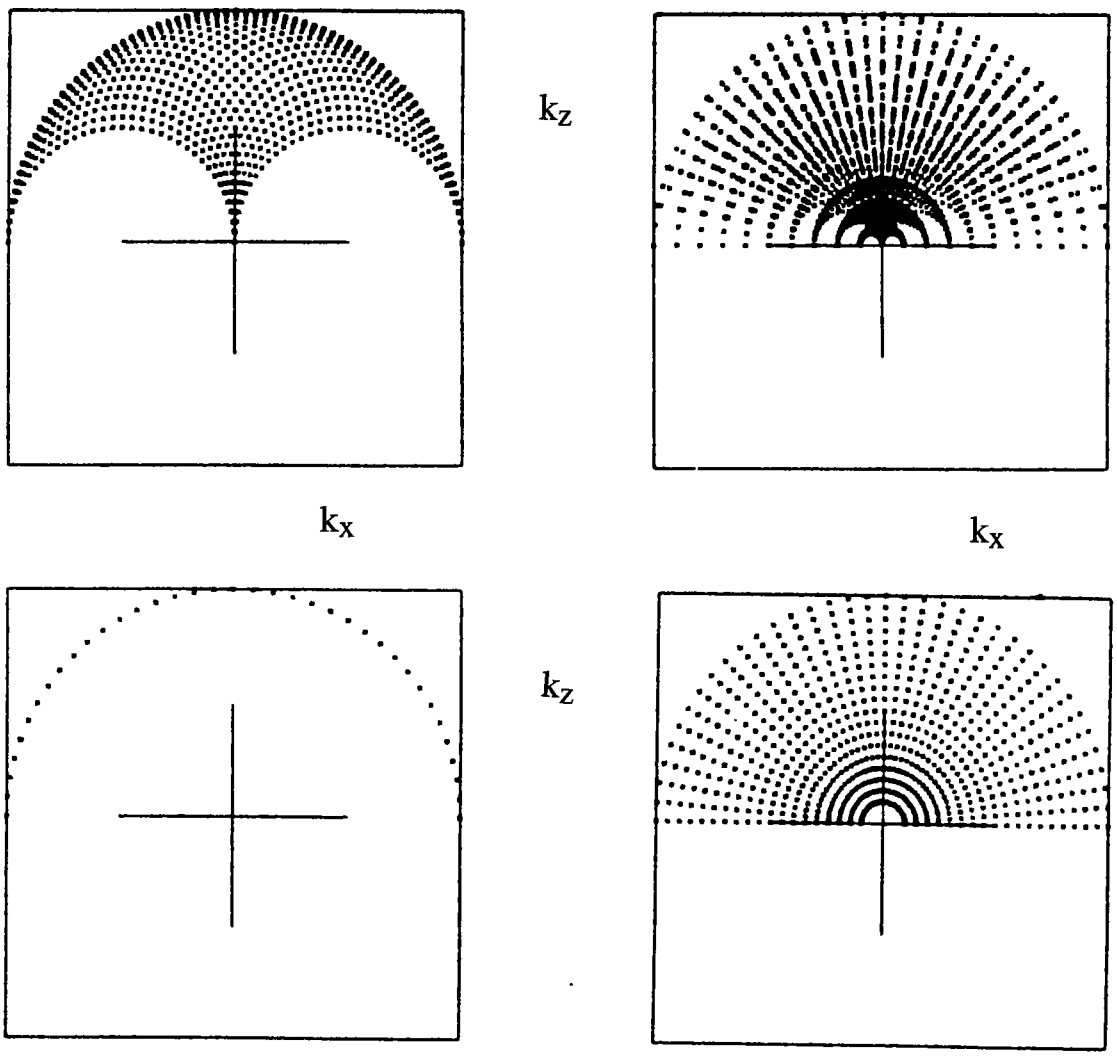

Figure 5. Fourier support area for surface reflection imaging. (a) multi-view at a single frequency; (b) multi-view with multi-frequency; (c) single frequency monostatic backscattering (θ=180 degs.), and (d) multi-frequency monostatic backscattering.

VERTICAL SEISMIC PROFILING

The vertical seismic profile (VSP) is a combined surface and borehole geometry. The typical configuration has sources located across the surface and receivers placed vertically down a borehole as illustrated in Figure 1b. As such, the VSP lies between surface-to-surface and crosswell in absolute spatial bandwidth and seismic resolution. Angles of incidence range from 0 degrees to -180 degrees, and angles of observation from -90 degrees to +90 degrees. In Figures 6a and 6b, I show results for single frequency and multi-frequency coverage, respectively. The differences lie in the sampling pattern and the limits of coverage. Overall coverage is similar thus suggesting that multiple frequencies do not offer as much advantage as in the case of surface reflection imaging.

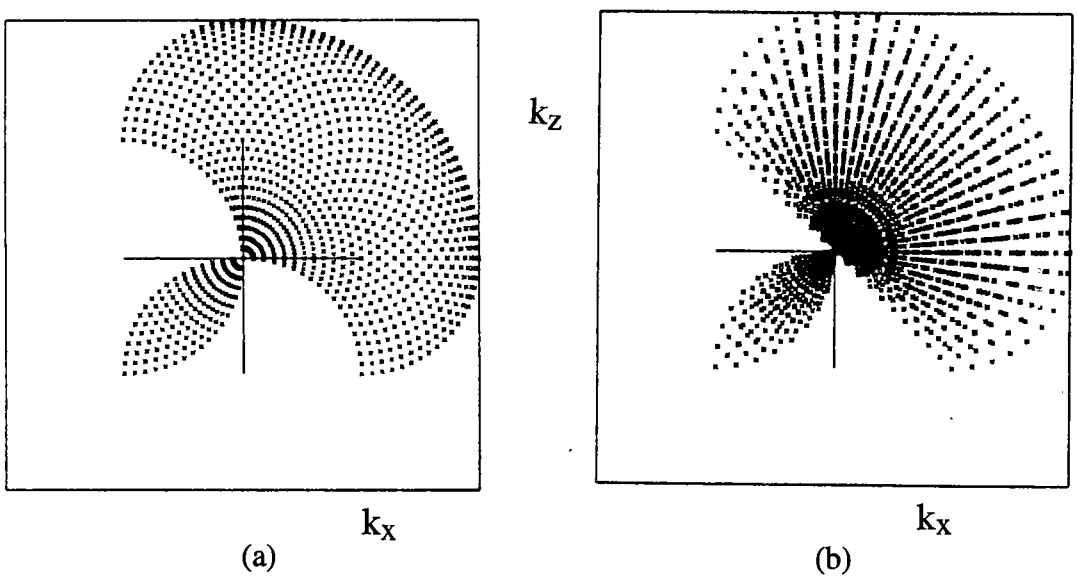

Figure 6. Fourier support area for vertical seismic profiling. (a) multi-view at a single frequency; (b) multi-view with multi-frequency.

CROSSWELL SEISMIC PROFILING

Our last geotomography configuration is the crosswell geometry illustrated in Figure 1c. The conventional arrangement is to place a vertical array of sources in one borehole and an array of receivers in another borehole. The angle of incidence ranges for -90 degrees to +90 degrees, and the angles of observation from +90 degrees to +270 degrees. The conventional single frequency multi-view spectrum is shown in Figure 7a. There are no samples along the horizontal k_x-axis, which means that infinite vertical layers cannot be resolved. Devaney {5} was the first to illustrate this. Multi-frequency observations with this view pattern gives the identical support area as shown in Figure 7a. Therefore, no fundamental advantage exists in making wideband crosswell measurements.

However, as shown in Figure 7b, the coverage can be significantly expanded by locating sources and receivers in the same borehole and making single-well backscattered measurements. This spectrum is exactly like the surface result shown in Figure 5a only with the axes exchanged. To completely fill out the Fourier plane, one would use the single frequency combination of forward scattering (Figure 7a) and backscattering (Figure 7b) from both wells; this yields the coverage illustrated in Figure 8c.

Alternatively, one could combine multiple frequencies from limited views, e.g., multi-frequency backscattering (θ=180) from both boreholes. This yields the support area illustrated in Figure 7d. This coverage is produced by the same monostatic technique used in obtaining Figures 5c and 5d for the surface geometry.

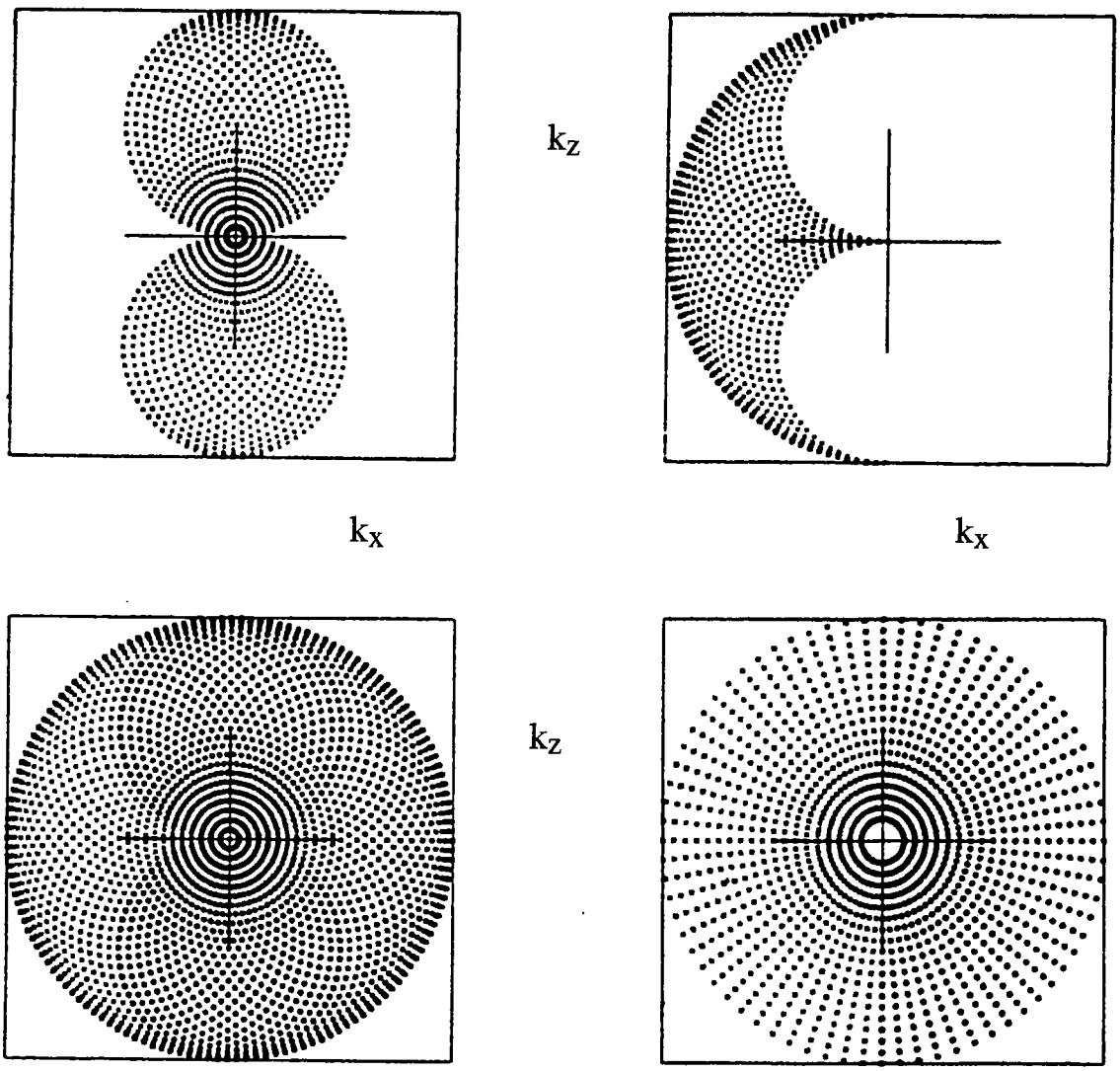

Figure 7. Fourier support area for crosswell seismic profiling. (a) multi-view at a single frequency forward scattering; (b) multi-view with multi-frequency; (c) single frequency monostatic backscattering (θ=180 degs.), and (d) multi-frequency monostatic backscattering.

ELASTIC WAVE IMAGING

Next, I turn attention to vector wavefields, in particular elastic waves. The basic theory for elastic wave scattering in the Born approximation is similar to that given in the section on modeling above. Nevertheless, it is necessary to reformulate the forward problem in order to identify the similarities and highlight the differences. The reader is referred to the paper by Gubernatis {8} for a detailed derivation of the results shown here.

Instead of Eqn. (7) for the scattered field, I have

$$U_{sc}(\mathbf{r},n) = A(\hat{\mathbf{s}},\hat{\mathbf{s}}';n,m)\exp(ikr)/r \tag{12}$$

$$A(\hat{\mathbf{s}},\hat{\mathbf{s}}';n,m) = k^2(4\pi)^{-1}U_o\, O_e(\mathbf{k}_{nm})Q(\mathbf{e}) \tag{13}$$

$$O_e(\mathbf{k}_s) = \int d\mathbf{r}'\, O_e(\mathbf{r}')\exp(-i\mathbf{k}_{nm}\cdot\mathbf{r}') \tag{14}$$

where $\mathbf{k}_{nm} = k_m\hat{\mathbf{s}} - k_n\hat{\mathbf{s}}'$, and the magnitude is $|\mathbf{k}_{nm}|^2 = k_n^2 + k_m^2 - 2k_nk_m\cos(\theta)$. Comparing (10) and (11) with (13) and (14), the similarities with the scalar and vector theories appear obvious. The notation does require some explanation. First, the subscripts "n" and "m" are used to denote the polarization of the scattered field, i.e., compressional or shear. The object profile $O_e(\mathbf{r})$ describes the perturbation in any one of the material constants (λ , μ, or ρ) , where the subscript "e" designates the constant. $Q(\mathbf{e})$ is a multipole factor which describes the polarization structure of the scattered fields. For weak scattering, $Q(\mathbf{e})$ is particularly simple containing no more than a monopole, a dipole, and a quadaruple. The far-field radiation patterns of the $Q(\mathbf{e})$ factor are illustrated in Figure 8. Thus, in (12) $U_{sc}(\mathbf{r}, n)$ is the scattered wave of mode "n" generated by the perturbation of type "e" from being excited by an incident wave of mode "m." The total scattered field is found by summing the contributions from all perturbations , all incident modes, and all scattered modes. The support area of the common mode (n=m) scattering spectra will be exactly like the scalar wave results shown above, except the amplitudes are further modified by the polarization factor. The spatial bandwidth will be different for compressional waves (n=P, m=P) and shear waves (n=S, m=S) because the wavelength at a given frequency in the background medium would be different.

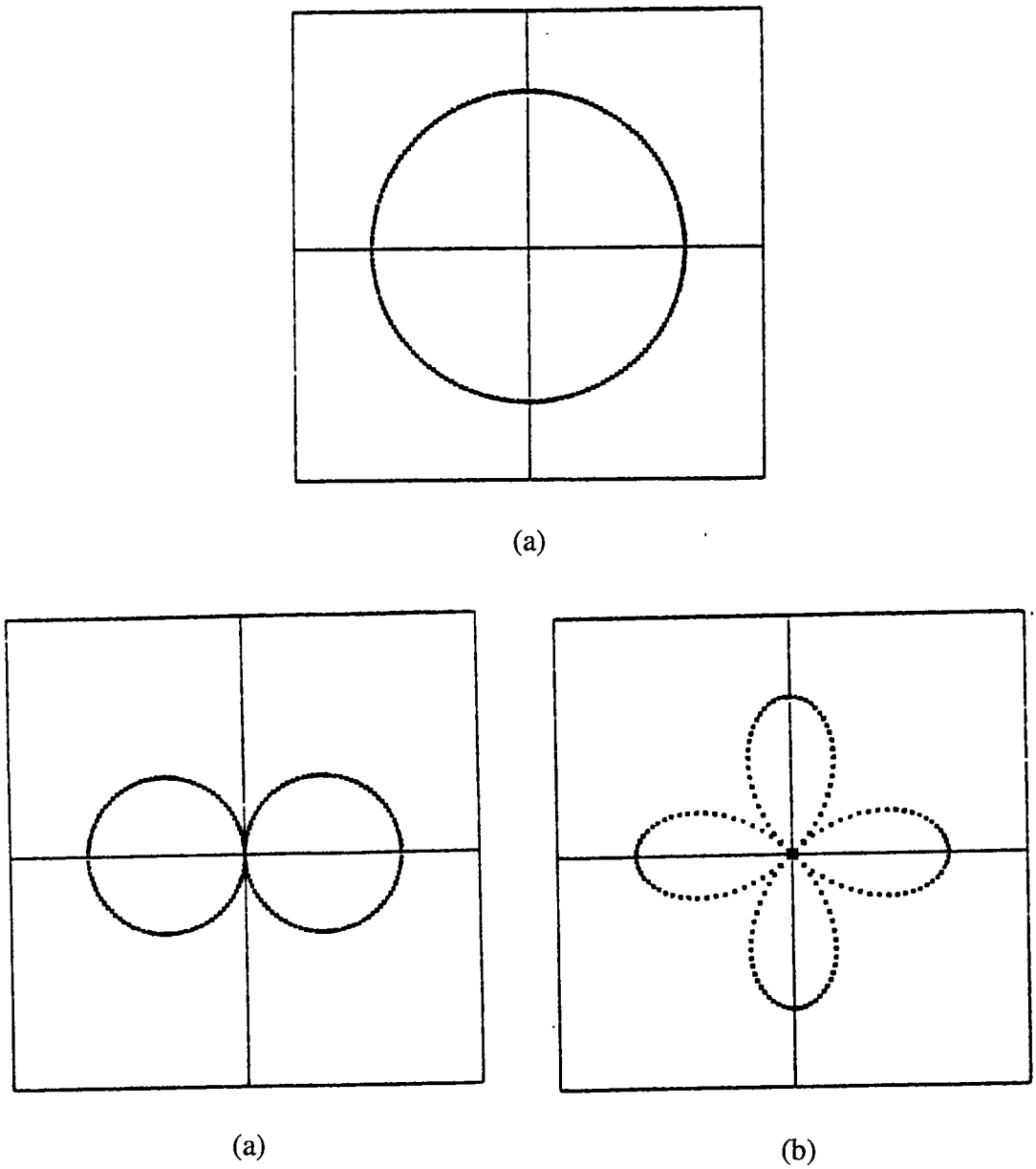

Figure 8. Radiation patterns for the three lowest order multipoles. (a) monopole, (b) dipole, (c) quadrapole.

The more interesting situation occurs for converted waves, e.g., compressional to shear. The effects are revealed through examination of the wavenumbers k_n and k_m. In

the remainder of this section, I show the Fourier support area for elastic converted waves for the three geophysical applications. The spectra are obtained by varying the frequency, angle of incidence, angle of observation, or the polarization. I do not show all possible cases but give representative examples. These examples are computed for a V_P/V_S ratio of 2.

I show the surface reflection support for compressional-to-shear scattering at a single frequency in Figure 9a. The structure of the support area is similar to that of Figure 5a except for the absence of samples near the origin and the appearance of samples along the k_x-axis. For near forward angles of scattering, the vectors $k_n\hat{s}$ and $k_m\hat{s}'$ no longer cancel each other. Converted wave coverage for the single frequency VSP is shown in Figure 9b.

Perhaps the most interesting example is the full aperture crosswell configuration shown in Figure 9c. This result illustrates how converted waves can be used to sample the horizontal k_x-axis which, of course, is missed by scalar or common mode imaging. An important point which can't be over-emphasized, is that common mode and converted mode waves are sensing different material properties so that one measurement is not a substitute for the other, but instead is complementary. Also, I note that the converted wave patterns shown here do not contain the amplitude of the sampled spectrum related to the multipole.

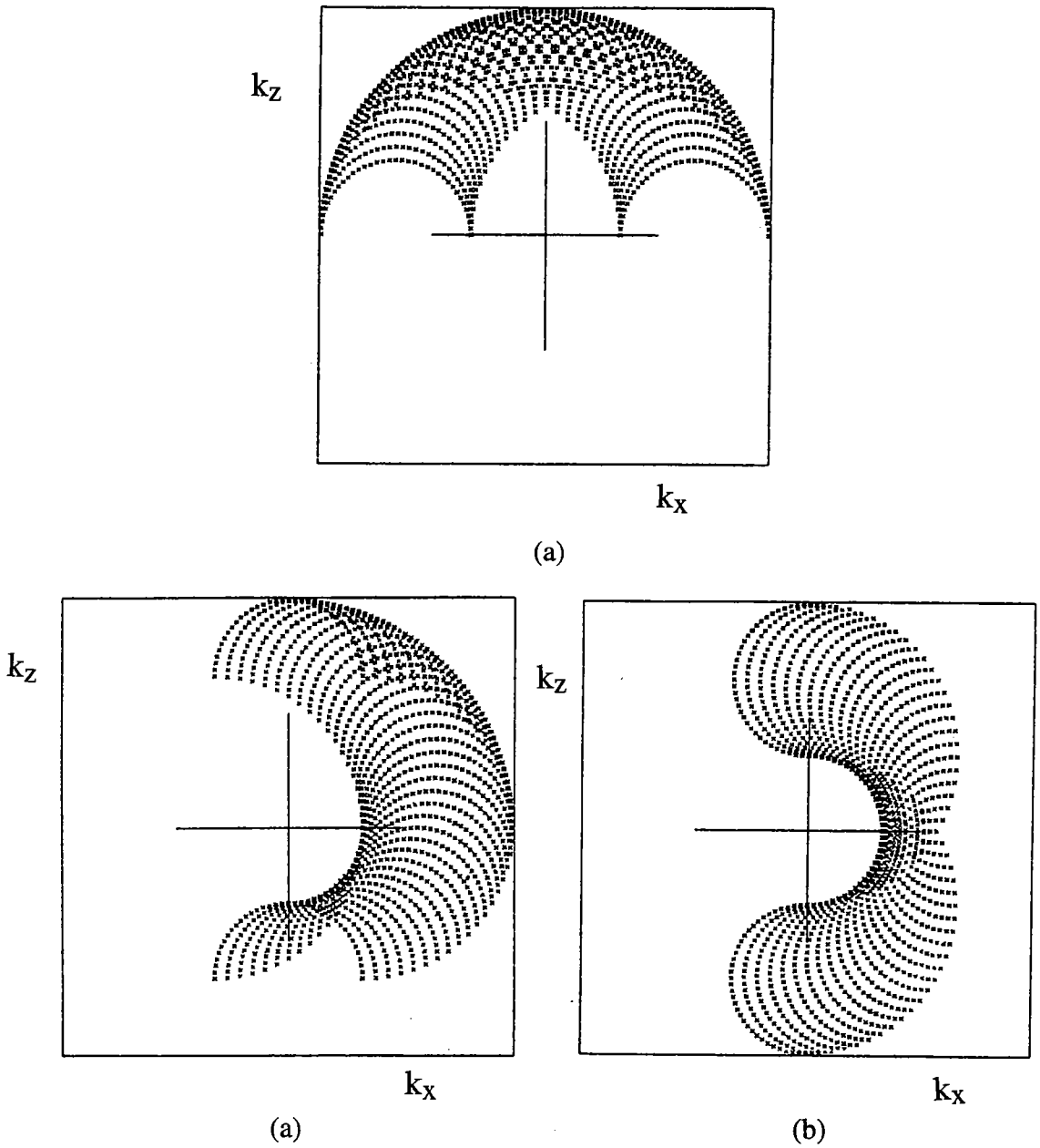

Figure 9. Fourier support area for P-to-S converted waves for multi-view single frequency (a) surface reflection profiling, (b) vertical seismic profiling, (c) crosswell seismic profiling. Vp/Vs ratio = 2.

CONCLUSIONS

I have shown several insightful yet simple illustrations of the support space of the geological spectrum sampled by geotomography. I have considered frequency, view, and polarization diversity as means for achieving spatial bandwidth. Most earlier work considered only view diversity. My results were obtained using a combined theoretical and phenomenological approach to the theory of diffraction tomography. This procedure proved to be convenient for examining vector as well as scalar waves. The important conclusion to be drawn from this work is that the spatial bandwidth required for imaging is achieved with "apparent" wavelengths, which are the projection of the true longitudinal signal wavelengths onto object space. The apparent wavelengths can be obtained by varying the angle of incidence, angle of observation, the frequency, and in some cases the polarization of the probing waves.

The major shortcoming of this work is the assumption that the object profile is weak and imbedded in a homogeneous constant background medium. Depending on the strength of the inhomogeneities, our results may be changed. However, one would expect the general structure of the support regions to remain similar to those presented here.

REFERENCES

[1] R. M. Lewitt, "Reconstruction Algorithms: Transform Methods," Proc. IEEE, vol 71, no. 3, pp. 390-408, March 1983.

[2] R. K. Mueller, et al., "Reconstructive Tomography and Applications to Ultrasonics," Proc. IEEE, vol 76. no. 4, April 1979.

[3] J. K. Greenleaf, "Computerized Tomography with Ultrasound," Proc. IEEE, vol 71, no. 3, March 1983.

[4] A. J. Devaney, "A Filtered Backpropagation Algorithm for Diffraction Tomography," Ultrasonic Imaging, vol 4, pp. 336-360, 1982.

[5] A. J. Devaney, "Geophysical Diffraction Tomography, " IEEE Trans. Geoscien. Remote Sens., vol. Ge-22, no. 1, pp. 3-13, Jan 1984.

[6] S. K. Kenue and J. F. Greenleaf, "Limited Angle Multifrequency Diffraction Tomography," IEEE Trans. Sonic Ultrason., vol. SU-29, no. 8, pp. 213-217, July 1982.

[7] E. Wolf, "Three-Dimensional Structure Determination of Semi-Transparent Objects from Holographic Data," Opt. Commun., vol 1, no. 4, pp. 153-156, 1969.

[8] J. E. Gubernatis, et al, "The Born Approximation in the Theory of the Scattering of Elastic Waves by Flaws," J. Applied Physics, vol. 48, no. 7, pp 2812-2819, 1977.

[9] J. M. Harris, "Diffraction tomography with arrays discrete Sources and receivers," IEEE Trans. on Geoscienceand Remote Sensing, vol. GE-25, No. 4, July, pp.448-455.

[10] M. Slaney and A. Kak, "Limitations of imaging with first-order diffraction tomography," IEEE Trans. Microwave Thy. Techs., vol. MTT-32, no. 8 August 1984.